ACS APPLIED

# Cu-Doped Layered Double Hydroxide Nanotubes For CO<sub>2</sub> Reduction under Supercritical Conditions

Alexandre C. Teixeira, Bruno Manduca, Adolfo L. Figueredo, Alysson F. Morais, Renato S. Freire, Pedro Vidinha, and Danilo Mustafa\*



Cite This: https://doi.org/10.1021/acsanm.5c03394

NANO MATERIALS



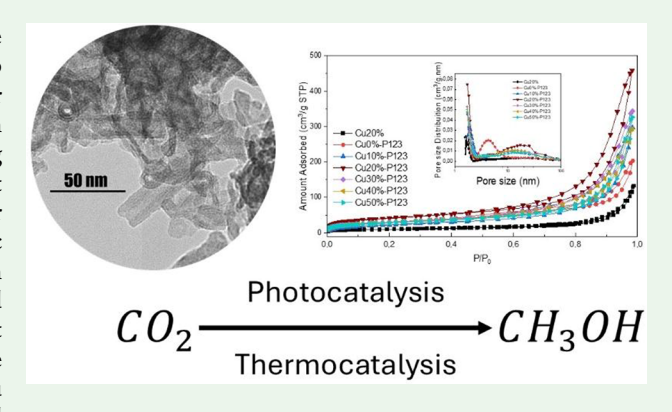
**ACCESS** I

Metrics & More

Article Recommendations

Supporting Information

ABSTRACT: Layered double hydroxides are structurally versatile materials whose chemical and electronic properties can be tuned to yield efficient heterogeneous catalysts and catalyst precursors for green chemistry applications, including sustainable fuel production for the methanol economy. We demonstrate that chemical tailoring via copper incorporation into ZnAlEu LDHs, combined with soft templating using a P-123 surfactant, yields well-defined nanotubular structures with markedly enhanced thermo- and photocatalytic performance in CO<sub>2</sub> hydrogenation to methanol. Eu<sup>3+</sup> incorporation enabled the nanotubular morphology and induced a 5-fold enhancement in the surface area of the LDHs, while subsequent Cu doping introduced active catalytic sites and further increased the surface area, reaching a maximum of 184 m<sup>2</sup>.g<sup>-1</sup> at an optimal Cu loading of 20%. Under visible light, these materials demonstrated



methanol yields significantly higher than nonhierarchical, flake-like LDHs, with a high selectivity attributed to the extended residence time of intermediates within the interlayer spaces. Thermocatalytic CO2 hydrogenation in flow reactors further confirmed the superior activity and selectivity of the Cu20%-P123 catalyst, achieving a methanol yield of 55 mg·g<sub>at</sub><sup>-1</sup>·h<sup>-1</sup>, outperforming conventional Cu-ZnO-Al<sub>2</sub>O<sub>3</sub>-based catalysts. These findings highlight the critical role of composition tuning and morphology control in enhancing the catalytic activity of LDH-based materials, offering a promising route for the sustainable valorization of CO2.

**KEYWORDS:** layered double hydroxide, nanotubes, CO<sub>2</sub> reduction, catalysis, copper

# 1. INTRODUCTION

The rising atmospheric CO<sub>2</sub> levels have created an urgent global imperative to mitigate their impact on climate change. As a result, significant efforts have been directed not only at reducing CO<sub>2</sub> emissions but also at utilizing it as a feedstock to produce sustainable fuels and chemicals. Among these, the hydrogenation of CO<sub>2</sub> to methanol has emerged as a promising strategy, aligning with the methanol economy principles and benefiting carbon recycling and the energy transition.<sup>2-4</sup> Despite extensive research, achieving high efficiency and selectivity toward methanol remains challenging. This difficulty is particularly evident in the Cu/ZnO/Al<sub>2</sub>O<sub>3</sub>-based (CZA) catalytic process for CO<sub>2</sub> hydrogenation. Dominant in industry, these processes still lead to undesirable side reactions, such as the reverse water-gas shift (RWGS) reaction and water-induced deactivation caused by active-site aggregation,5-7 the former leading to a decrease in methanol selectivity.

Catalyst efficiency in CO<sub>2</sub> reduction critically depends on the availability of high-surface-area materials with accessible electrons at the energy levels required to drive the reaction.<sup>8,9</sup> Accessible catalytically active electronic states can be introduced by doping metal sites such as copper, rhenium, indium, or other metallic structures into nanoparticles or nanoporous frameworks, where the large surface area enhances exposure of catalytic centers. <sup>10,11</sup> For instance, smaller Cu nanoparticles increase site exposure and suppress side reactions, thereby improving methanol selectivity compared to larger ones. <sup>12–14</sup> Likewise, the morphology and composition of the support material strongly influence catalytic activity, stability, and electron transfer dynamics. 15-18

The development of new advanced catalysts with optimized nanoparticle morphology and chemical composition is critical to overcoming the efficiency and selectivity challenges of  $CO_2$  hydrogenation. Layered double hydroxides (LDHs) are versatile materials with tunable chemical composition and extensive morphological flexibility, offering a versatile platform

Received: July 23, 2025 Revised: October 8, 2025 Accepted: October 13, 2025



for catalytic CO<sub>2</sub> conversion. 22-27 They are intrinsically microporous materials formed by positively charged mixed metal hydroxide layers interlayered by hydrated anions (An-.yH2O). Their hydroxide layers have chemical formula  $[M_{1-x}^{II}M_x^{III}(OH)_2]^{x+}$ , where  $M^{II}$  and  $M^{III}$  represent, respectively, di- and trivalent metals. 28-31 LDHs have emerged as promising materials for photocatalytic applications due to their tunable composition and ability to facilitate charge separation. 32-34 Using different divalent, trivalent, and tetravalent metals (e.g., Zn<sup>2+</sup>, Mg<sup>2+</sup>, Co<sup>2+</sup>, Ni<sup>2+</sup>, Al<sup>3+</sup>, RE<sup>3+</sup>, Cr<sup>3+</sup>, Ga<sup>3+</sup>, Ti<sup>4+</sup>, and Ce<sup>4+</sup>), LDH photocatalysts with tailored absorption and catalytic activity have been reported. 35,36 Their versatility is also reflected in Ru-loaded MgAl-LDHs for CO2-to-formic acid conversion<sup>22</sup> and Cu-Fe LDH-derived catalysts for long-chain hydrocarbon production.<sup>25</sup> Beyond hydrogenation, LDHs have shown capacity for CO<sub>2</sub> capture and direct photocatalytic reduction, as demonstrated with LiAl<sub>2</sub> and Zn-Cu-Ga systems. <sup>25,37</sup> Nanostructured LDHs further improve activity by exposing more active sites, achieving up to 300-fold higher performance compared to bulk materials<sup>38</sup>

Recently, well-defined, multiwalled, hollow cylindrical ZnAlEu LDH nanotubes were reported. 28,42,43 They can be obtained through the controlled hydrolysis of metal ions (Zn<sup>2+</sup>, Al<sup>3+</sup>, and Eu<sup>3+</sup>) in the presence of 1,3,5-benzenetricarboxylate (BTC) anions and nonionic Pluronic P-123 worm-like micelles. The incorporation of Eu<sup>3+</sup> ions plays a critical role in directing the self-assembly process, as they facilitate the precipitation of LDH layers onto the convex surfaces of the micellar template. This results in the formation of hierarchical nanotubular structures with well-defined mesoporosity and enhanced surface area. In this context, Zn<sup>2+</sup> and Al<sup>3+</sup> provide a stable LDH framework, while Eu3+ has been shown to incorporate into the brucite-like layers, distorting the hydroxide sheets and facilitating nanotube formation. EXAFS analysis confirmed that Eu<sup>3+</sup> is accommodated in the LDH lattice rather than segregated into Eu-rich phases, which explains its crucial role in enabling the hierarchical morphology. 28,44 Thus, the Zn/Al/Eu composition provides the structural platform upon which Cu can be introduced as the catalytically active component.

Here, we show that this new nanotubular morphology provides a robust framework for advanced catalytic applications. Combining the nanotubular morphology with the versatility in chemical composition of the LDHs, high surface area, Cu-doped LDH nanotubes have been synthesized for the first time, serving as efficient catalysts for CO<sub>2</sub> reduction under supercritical conditions (Figure 1). Upon optimization of their

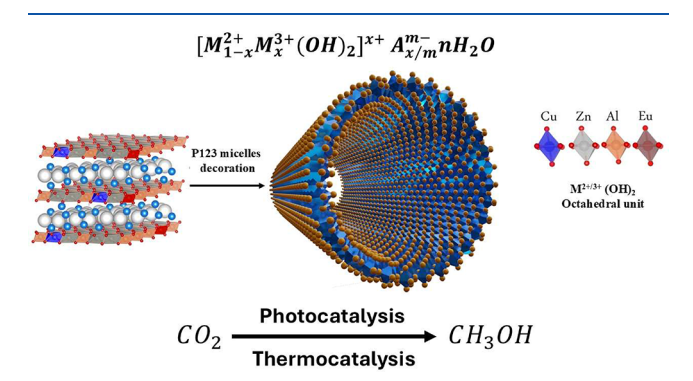


**Figure 1.** Structure and chemical composition of Cu-doped Zn/Al/Eu LDH and its nanotubular morphology.

Cu content, the LDH nanotubes demonstrated methanol yields six times higher than those of 2D LDHs, achieving a yield of 28 mmol<sub>MetOH</sub>.g<sub>cat</sub><sup>-1</sup>. Beyond photocatalysis, thermocatalytic CO<sub>2</sub> hydrogenation in flow reactors underscored the superior performance of the Cu-doped nanotubular LDH catalysts, achieving a methanol yield of 55 mg·g<sub>at</sub><sup>-1</sup>·h<sup>-1</sup>—well above that of standard Cu-ZnO-Al<sub>2</sub>O<sub>3</sub> catalysts, highlighting its promise for scalable CO<sub>2</sub>-to-methanol conversion. It is important to emphasize that the focus of this work lies on the synthesis and structural characterization of the Cu-doped nanotubular LDH for catalysts; therefore, aspects such as postreaction stability or long-term durability are beyond the intended scope of this study.

#### 2. MATERIALS AND METHODS

- **2.1. Materials.** The metal precursor salts  $Zn(NO_3)_2.6H_2O$  (96%, LabSynth),  $Al(NO_3)_3.9H_2O$  (98%, LabSynth),  $Cu(NO_3).3H_2O$  (98%, LabSynth), the organic acid  $H_3BTC$  (benzene-1,3,5-tricarboxylic acid, 97 mol %, Sigma-Aldrich), the triblock copolymer Pluronic P-123 (Sigma-Aldrich), and NaOH (97 mol %, Vetec) were procured and used without further purification.  $Eu(NO_3)_3.6H_2O$  was synthesized via the addition of nitric acid in an  $Eu_2O_3$  (CSTARM, 99% China) precursor. 45
- 2.2. Synthesis of Flake-Like LDHs. LDHs were prepared accordingly to the coprecipitation method described by Moraes et al. 42 Initially, one aqueous solution containing the dissolved nitrates precursors of the metals Zn<sup>2+</sup>, Cu<sup>2+</sup>, Al<sup>2+</sup>, and Eu<sup>3+</sup> was prepared in 10 mL of DI. The divalent metals were incorporated in the LDH using the following molar ratios  $(Cu^{2+}/(Cu^{2+}+Zn^{2+}) = 10\%, 20\%, 30\%,$ 40%, and 50%. In addition to the incorporation of  $Cu^{2+}$ , the  $Eu^{3+}$ assumed the  $Eu^{3+}/(Eu^{3+} + Al^{3+}) = 15\%$  molar ratios, which proved to be the best proportion for the formation of the tubes. Hereafter, 10 mL of metal solution was added dropwise (~10 mL.h<sup>-1</sup>) into 200 mL of a likewise aqueous solution containing the dissolved BTC anions in adequate concentrations to neutralize the positive charge of the hydroxide layers. The pH was kept around 8 by dosing a 1 mol·L<sup>-1</sup> NaOH solution with the automatic titrator Metrohm 848 Tritrino plus. The resulting solution was aged statically for 2 days at 60 °C, centrifuged, washed with distilled water, and dried in an oven at 60 °C for 3 days. The final solid was ground to produce a fine powder.
- 2.3. Synthesis of LDH Nanotubes. In order to obtain nanotubes, cylindrical micelles needed to be prepared first. In this case, 0.15 wt % of P123 was dissolved in 200 mL of aqueous solution under 400 rpm magnetic stirring at 60 °C. After complete dissolution, BTC was added to the solution, and the pH was adjusted to 6. After its dissolution, the solution was cooled down to room temperature, reheated to 60 °C, and finally cooled down again to room temperature to optimize the formation of micelles (cycle process). To this solution, the metal solution was added dropwise, likewise for the flake-like LDH. This time, after the 2 days aging at 60 °C, the P123 was removed from the material by washing the centrifuged precipitant with methanol in a sonicated bath. The last step was drying at 60 °C for 3 days. For the samples used to evaluate its catalytic properties, an extra step was introduced to further remove any methanol contamination from the material. In this case, the resulting powder was placed in an oven at 100 °C for 24h. The Supporting Information (SI) provides a flowchart of the preparation of nanotubes (Figure S1).
- **2.4. Physicochemical Characterization.** The chemical compounds of LDH were determined using coupled plasma optical emission spectroscopy (ICP-OES). X-ray diffraction (XRD) measurements were obtained using a D8 Discover (Bruker, Atibaia, Brazil) diffractometer in Bragg—Brentano geometry using Cu K $\alpha$  radiation ( $\lambda$  = 1.54 A). Data were recorded from 4° to 70° (2 $\theta$ ) with steps of 0.05° using a counting time of 1s per step. Using the most intense direction (003), the crystallography parameters were obtained information about the structure of LDH using Bragg's law,  $n\lambda$  = 2dsin $\theta$ , and as full width at half-maximum (fwhm) data using the Scherrer equation: L =

 $K\lambda/\beta\cos\theta$ . The morphology was obtained by transmission electron microscopy (TEM). Fourier transform infrared (FTIR) spectra were recorded in the range from 400 to 4000 cm<sup>-1</sup> in a PerkinElmer Frontier FT-IR spectrometer using pellets of samples embedded in KBr. Diffuse reflectance spectra were acquired in a Shimadzu UV-2550 UV-vis spectrophotometer equipped with a DRS module, in the range from 200 and 800 nm and step of 0.5 nm. The powder materials were supported in BaSO<sub>4</sub>. Photoluminescence excitation and emission spectra were collected at room temperature using an FS5 spectrofluorometer (Edinburgh Instruments) equipped with a 150 W xenon arc lamp. The measurements were carried out in the solid state using a front-face geometry configuration, and spectral corrections were applied to both excitation and emission channels. N<sub>2</sub> adsorption isotherms were acquired in a Micromeritics ASAP 2010 device following a sample degassing for 2 h at 100 °C. From the adsorption data, the Brunauer-Emmet-Teller (BET) specific surface area of the samples was determined, and the pore size distribution was obtained using the Barrett-Joyner-Halenda (BJH) method. Temperature-programmed reduction (H2-TPR) analyses were conducted using an Autosorb IQ system equipped with ASiQwin software (Quantachrome Instruments). The experiments were performed in a chemisorption sample cell placed inside a tube furnace coupled to a thermal conductivity detector (TCD). Prior to reduction, the catalyst was pretreated at 100 °C for 30 min under a 100 mL min<sup>-1</sup> He flow. Subsequently, the temperature was increased from 50 to 950 °C at a heating rate of 10 °C min<sup>-1</sup>, under a mixture of 30 mL min<sup>-1</sup> N<sub>2</sub> and  $1 \text{ mL min}^{-1} \text{ H}_2$ 

**2.5. Photocatalytic Tests.** The photocatalytic experiments were conducted in a 15 mL stainless steel reactor with a sapphire window at the top. The temperature was maintained at 60 °C with a heating jacket. The light source was a 300W Xe lamp. 1 mL of ultrapure water was placed at the bottom of the reactor, while the catalysts (10 mg) were placed over a glass fiber membrane suspended at half the height of the reactor so that the materials were separated from the water. The system was purged with gaseous  $N_2$  (3 bar) and  $CO_2$  and then pressurized with  $CO_2$  up to 100 bar. The reactor was irradiated for 24 h with magnetic stirring. After that, 5 bar of the gaseous phase was collected and analyzed for CO and  $CH_4$ . The remaining was bubbled in 2 mL of ultrapure water in an ice bath to collect liquid products.

2.6. Thermocatalytic Tests. The thermocatalysis experiments were conducted in a cylindrical stainless steel batch reactor with a volume of 10 mL. Prior to the injection of H<sub>2</sub> and CO<sub>2</sub>, the reactor was purged with N<sub>2</sub> for 5 min. Utilizing 10 mg of catalyst, it underwent an in situ reduction at 300 °C for 1 h under 50 bar of H<sub>2</sub>. After prereduction, the partial pressure of H<sub>2</sub> was adjusted to 80 bar, and it was pressurized with CO2 to a total pressure of 100 bar. The reaction occurred for 20 h. At the end, 5 bar was collected for the quantification of gaseous products, and for the quantification of liquid products (alcohols), the reactor was depressurized into 2 mL of water. The products were quantified by gas chromatography (Stabilwax DA  $60\text{m} \times 0.25 \text{ mm} \times 0.25 \mu\text{m}$  capillary column from Restek). For the reaction in flow, a fixed-bed flow reactor was packed with 1200 mg of Cu20%-P123, which was prereduced in situ under pure H<sub>2</sub> under atmospheric pressure at 300 °C for 1 h. The heating ramp employed was 10 °C/min. A spring-loaded back-pressure valve was used to maintain the reaction pressure at 100 bar. The exit of the backpressure valve was connected to a GC System (Shimadzu GC-2030) for analysis of the reaction mixture, comprised of two thermal conductivity detectors (TCD) for gas products and one flame ionization detector (FID) for liquid products. The chromatographic columns used were Rt-Msieve 5A PLOT, Rt-Q-BOND PLOT, Rtx-1, and molecular sieve 5A.

#### 3. RESULTS AND DISCUSSION

**3.1. LDH Nanotubes and Their Structure and Morphology.** LDH nanotubes were prepared via coprecipitation of Zn<sup>2+</sup>, Cu<sup>2+</sup>, Al<sup>3+</sup>, and Eu<sup>3+</sup> in a solution containing P-123 worm-like micelles and benzene-1,3,5-tricarboxylate anions, as described elsewhere and detailed in the Supporting

Information. <sup>28,42</sup> The LDHs have an atomic metal fraction  $M^{II}/M^{III} = (Zn + Cu)/(Al + Eu)$  of 2. Eu<sup>3+</sup> was introduced in the synthesis of up to 15% of the  $M^{III}$  metals. The amount of Cu in the materials varied between 0 and 50% of that of the  $M^{II}$  metals. These samples were named CuA%-P123, where A = 0, 10, 20, 30, 40, and 50% stands for the nominal Cu/(Zn + Cu) fraction in the sample. An LDH with nominal Cu/(Zn + Cu) = 20% that was synthesized without soft templating was named Cu20%. The chemical composition of the samples was investigated via elemental analysis (ICP-OES) and is reported in Table S1. The actual elemental composition of each sample is in good agreement with its nominal composition.

The powder X-ray diffraction (PXRD) patterns of all samples show the typical pattern of LDHs phases (Figure 2),

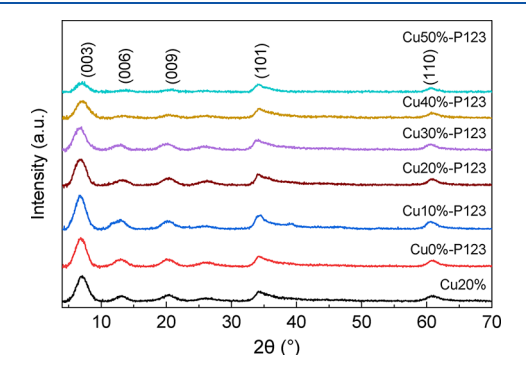


Figure 2. X-ray diffraction patterns of the LDH samples.

with no presence of crystalline side phases. The Bragg reflections below 30°  $2\theta$  are related to the periodic repetition of the hydroxide layers, while their broadness reflects the nanoscale size of the crystal in the stacking direction and the distortions created by the inclusion of Eu<sup>3+</sup> and Cu<sup>2+</sup> in the structure. The position of these peaks reveals an interlayer distance between 1.23 and 1.30 nm, consistent with the intercalation of the benzene-1,3,5-tricarboxylate anions used during synthesis to structure the nanotubes. Application of the Scherrer equation to analyze the crystalline domain size in the samples reveals a crystal size of around 4.3 nm in the stacking direction (Table S2). In the region between 30 and  $40^{\circ} 2\theta$ , a broad and asymmetric peak is observed, which is composed of multiple overlapping Bragg reflections. This overlap, common in nanosized LDH phases, prevents a full crystal structure determination. Notably, the intensity of the Bragg reflections decreases as the copper content in the structure increases. This effect is particularly pronounced for concentrations above 20% and is linked to the absorption of the X-ray beam in the  $CuK\alpha$ edge. The PXRD patterns of Cu-containing LDH showed no distinct reflections attributable to crystalline CuO or Cu2O phases, suggesting that if secondary phases are present, they are either highly amorphous or below the detection limit of the technique.

Transmission electron microscopy (TEM, Figure 3) was employed to investigate the morphological evolution of the materials upon increasing Cu concentration, particularly focusing on the formation of self-supported nanotubes. In the absence of copper (sample Cu0%-P123, Figure 3A,B), well-defined tubular structures are observed, as already described elsewhere. Addition of Cu up to Cu/(Zn + Cu) fractions of 20% (Figure 3D,E) retains the nanotubular morphology. The TEM micrographs clearly reveal the density contrast between the nanotube walls made of metal hydroxide

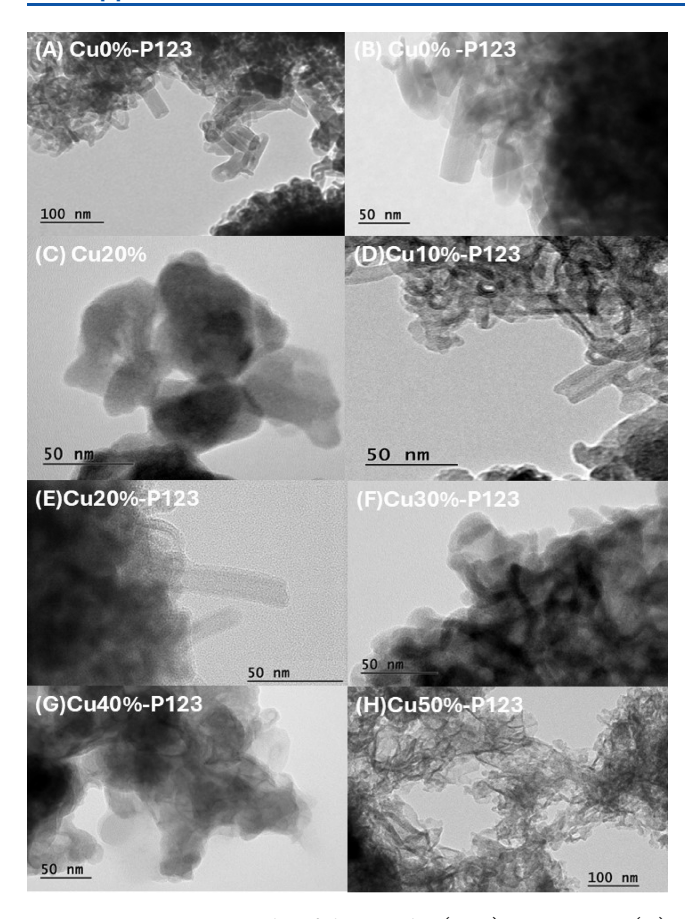


Figure 3. TEM micrographs of the samples (A, B) Cu0%-P123, (C) Cu0%, (D) Cu10%-P123, (E) Cu20%-P123, (F) Cu30%-P123, (G) Cu40%-P123, and (H) Cu50%-P123.

layers and the hollow mesopore in the middle of the nanotubes. The average outer and inner diameters of the nanotubes were determined to be 16.4 and 7.1 nm, respectively. When the Cu<sup>2+</sup> content exceeds 20% (e.g., 30, 40, and 50%) (Figure 3F,G), the formation of tubular morphologies is suppressed and the LDHs display exclusively a "twisted" or curled nanosheet morphology.

The porous structure of the samples was further investigated via Brunauer–Emmett–Teller (BET) analysis of their nitrogen adsorption–desorption isotherms, as shown in Figure 4. LDHs with plate-like morphology (Cu0%) present micropores related to the interlayer space in the region below 2 nm (see pore distribution curve in the inset of Figure 4) and have a relatively low specific BET surface area of 34 m $^2$ /g. A much larger BET specific surface area between 123 and 184 m $^2$ /g is observed for the nanotubes (Table 1). In addition to interlayer space, these

Table 1. Nitrogen Adsorption Data

| samples    | BET surface area $\left(m^2/g\right)$ | BJH pore volume $(cm^3/g)$ |
|------------|---------------------------------------|----------------------------|
| Cu20%      | 34.33                                 | 0.21                       |
| Cu0%-P123  | 123.00                                | 0.34                       |
| Cu10%-P123 | 128.66                                | 0.50                       |
| Cu20%-P123 | 183.76                                | 0.75                       |
| Cu30%-P123 | 143.80                                | 0.56                       |
| Cu40%-P123 | 132.99                                | 0.48                       |
| Cu50%-P123 | 126.78                                | 0.53                       |

materials feature mesopores related to cylindrical voids of the tubular morphology. These pores are seen in the pore distribution curves as a broad feature centered around 15 nm. Interestingly, a high BET specific surface area is also observed for the samples in which the nanotubular morphology has been suppressed due to an excessively high Cu concentration (Cu30%-P123, Cu40%-P123, and Cu50%-P123).

**3.2. Electronical Properties.** To investigate the electronic properties of the LDHs, selected samples were characterized by X-ray photoelectron spectroscopy (XPS), as shown in Figure 5. The samples analyzed included Cu0%-P123 and Cu20%-P123 after reduction and Cu20% both before and after reduction. The copper concentrations determined by XPS were lower than those measured by ICP-OES, indicating that most of the metal resides within the bulk of the material rather than on its surface. Additionally, the Cu concentration was found to be higher on the surface of the reduced materials. This behavior is typical of catalysts containing Cu, as the metal tends to migrate to the surface during the reduction process.<sup>46</sup>

The binding energies (BE) of Cu 2p suggest that Cu<sup>0</sup> is the predominant species on the surface of Cu20%, both before and

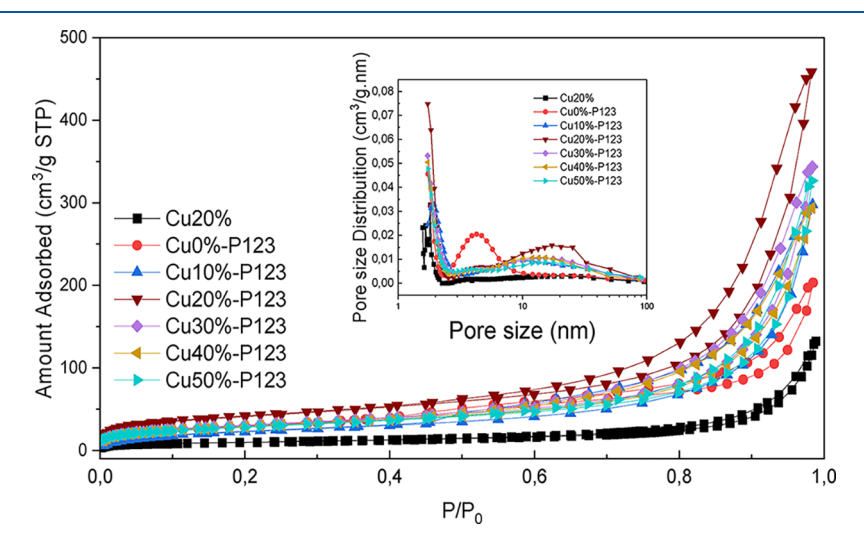


Figure 4. Nitrogen adsorption—desorption isotherms and the corresponding pore size distribution plots.

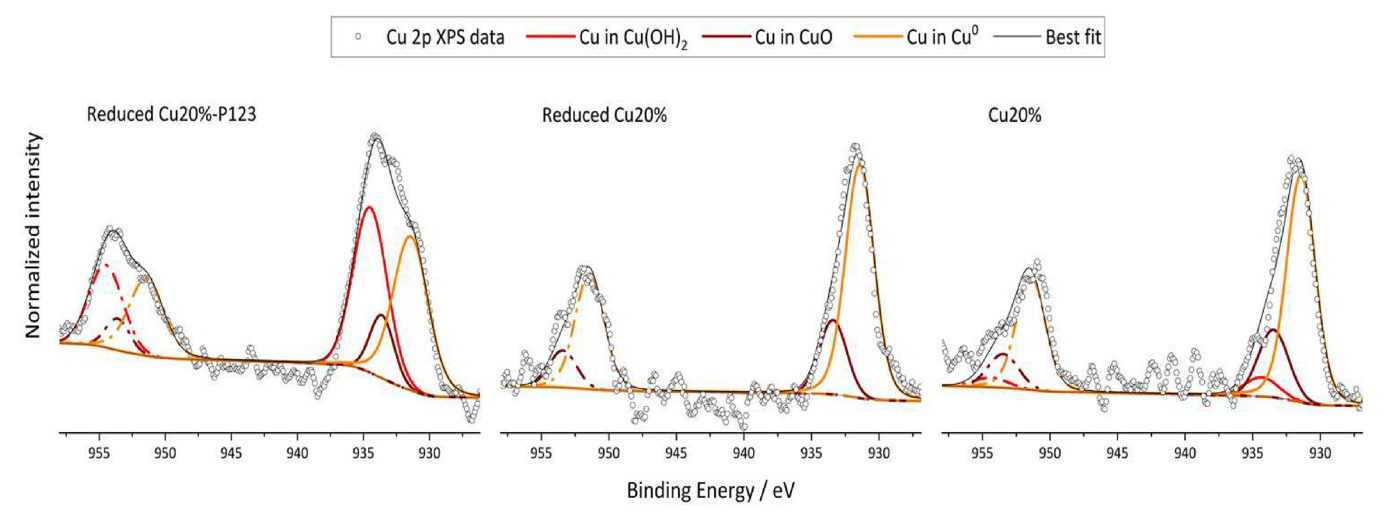


Figure 5. Cu 2p XPS spectra of reduced Cu20%-P123; reduced Cu20% and Cu20%. Full lines represent the 2p3/2 and dotted lines represent the 2p1/2 of each species.

after reduction. The increase in the surface Cu content after reduction may indicate partial migration of copper species toward the surface. Although this effect was not investigated in detail here, it is consistent with the known tendency of Cu to segregate under reducing conditions in the LDH-derived catalysts. In contrast, the Cu20%-P123 sample exhibits a mixture of Cu(OH)<sub>2</sub>, CuO, and Cu<sup>0</sup>, as summarized in Table S3. These findings highlight the impact of both the reduction process and the use of P123 in influencing the surface composition and oxidation state of copper in the materials. Although the binding energies of Cu<sup>+</sup> and Cu<sup>0</sup> are close and can overlap in the Cu 2p region, we relied on the Cu 2p fine spectra for qualitative discussion. The Cu LMM Auger region could not be used reliably in our case due to low signal resolution and interference from Zn Auger lines in the same energy range. Nonetheless, this approach is widely employed in the literature to discuss copper oxidation states in CuZn-based LDH catalysts. The XPS also confirmed the presence of Eu<sup>3+</sup> in all materials. The BE of Zn  $2p_{1/2}$  in Cu20%-P123 (1022,09 eV) is higher than that in Cu0%-P123 (1020,51 eV). This indicates the incorporation of Cu in the LDH lattice. 47 Table S4 shows the elemental concentrations of each sample.

**3.3. Reduction Properties.** To investigate the reducibility of the metal species and their interaction with the support, the materials were analyzed by H<sub>2</sub>-TPR. The ease with which Cu<sup>2+</sup> species are reduced to metallic copper (Cu<sup>0</sup>) is a crucial indicator of their availability and potential catalytic activity. The H<sub>2</sub> consumption profiles for all samples are presented in Figure 6. A comparative analysis of the profiles reveals distinct differences in the reduction temperatures, which can be attributed to both the material's morphology and the copper content incorporated into the structure.

Despite the low signal intensity compared to that of the other materials, the Cu0%-P123 sample shows a very broad, low-intensity peak at a high temperature, centered at approximately 500-550 °C. The signal is related to the partial reduction of the LDH support itself, which is composed of zinc, aluminum, and europium. Most likely, this peak corresponds to the reduction of a small fraction of Zn<sup>2+</sup>ions present in the mixed oxide structure.

In the copper-containing catalysts, such as Cu10%-P123 and Cu20%, the reduction peaks observed in the same temperature

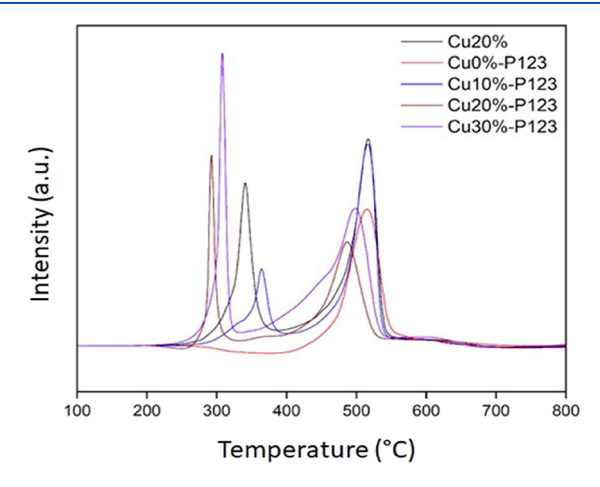


Figure 6. H<sub>2</sub>-TPR profiles of the LDH samples.

range (above 490  $^{\circ}$ C) are much more intense. This indicates that although the reduction of the zinc support is also occurring, the signal is predominantly dominated by the reduction of copper species that are strongly integrated into the LDH structure.

The Cu20% sample shows two reduction peaks, at  $\sim\!335$  and  $\sim\!515$  °C. Since XRD analysis rules out the presence of a separate CuO phase, both peaks must correspond to Cu²+ions incorporated into the LDH structure. The high-temperature peak ( $\sim\!515$  °C) can be attributed to Cu²+ ions that are strongly integrated into the hydroxyl layers, substituting Zn²+ in a more ordered lattice, which requires higher energy for their reduction.  $^{48}$  The low-temperature peak ( $\sim\!335$  °C) likely corresponds to Cu²+ ions located in more accessible sites with lower coordination, such as at the edges of the lamellae or at defect sites within the structure.  $^{49,50}$ 

In contrast, Cu20%-P123 shows a different profile with an intense reduction peak at a much lower temperature ( $\sim$ 290 °C). XRD analysis indicates that copper incorporation causes structural disorder. This disorder, combined with the high surface area of the nanotubular morphology (184  $m^2/g$ ), creates a large population of Cu<sup>2+</sup> ions in highly distorted environments with strained M–O–M bonds and greater surface exposure. These "disordered" sites are energetically less stable and, therefore, much easier to reduce, which explains the

appearance of the intense peak at 290 °C. This result is a signature of a highly active copper species. The second peak, at  $\sim$ 495 °C, still represents copper that is more integrated into the structure, but its reduction is facilitated (at a lower temperature than in Cu20%) due to the nanometric and strained nature of the tube walls.

The comparison among the nanotubular samples with 10, 20, and 30% copper reinforces this interpretation. As the copper content increases to 20%, the temperature of the first reduction peak drops from ~370 to ~290 °C. This aligns perfectly with the XRD observation that increasing the copper content intensifies the structural disorder. Therefore, a higher copper concentration generates more defective and strained sites, resulting in more reducible copper species. However, an increase to 30% copper induces a reduction in the material's tubular structure, which can contribute to lower Cu dispersion and a smaller surface area, leading the Cu species to reduce at higher temperatures compared to Cu20%-P123.

**3.4. Photocatalytic CO<sub>2</sub> Reduction.** The photocatalytic CO<sub>2</sub> reduction was evaluated under visible light irradiation of a 300W Xe lamp through a 10 mm thick sapphire window. Control experiments were conducted in the dark and in the absence of a catalyst. No reduction products were detected under these control conditions. Under light irradiation, only the formation of alcohols could be observed. Supercritical CO<sub>2</sub> enhances photocatalytic hydrogenation by increasing CO<sub>2</sub> concentration at active sites through its high density. The low viscosity improves the mass transfer and diffusion rates of reactants and products. It also enhances the water solubility. A test reaction using a Cu<sub>2</sub>O-P123 catalyst at 25 bar (non supercritical conditions) yielded 5.71 μmol·g<sup>-1</sup> of methanol.

Figure 7 shows the results of the photocatalytic experiments. The product formation increases with the Cu concentration

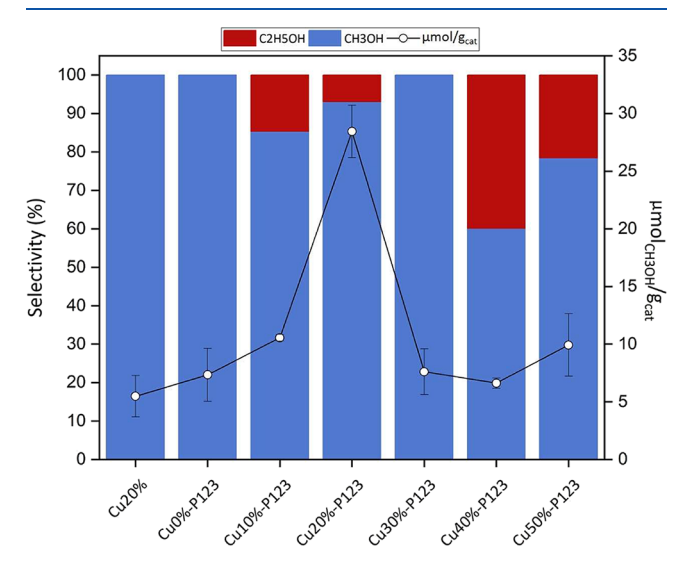


**Figure 7.** Alcohols selectivity and yield production at various cooperbased catalysis. Reactions: 100 bar, 60 °C, 10 mg of catalyst and 24 h.

until Cu20%-P123. These results indicate that both structure and Cu content play a role in the  $CO_2$  reduction. When comparing Cu20% with Cu20%-P123, it is possible to see a great influence of the tubular structure on the product formation, since its methanol formation (28.4  $\mu$ mol/g) is almost seven times higher than the flake counterpart (4.2  $\mu$ mol/g). The decrease in alcohol formation over the Cu30%-

P123 can be assigned to the lack of tube-like structures in this material.

Wein et al.<sup>54</sup> suggested that the high selectivity toward methanol in LDH photocatalysts can be attributed to the longer residence time of reaction intermediates within the interlayer spaces of the material. This extended residence time facilitates more efficient conversion processes. Additionally, the tubular morphology of the material can further enhance this effect as it increases the interaction time between the intermediates and the active sites, thereby contributing to even higher selectivity for methanol. Moreover, it was observed that Cu atoms are reduced by photogenerated electrons, subsequently transferring these electrons to CO<sub>2</sub>, facilitating its conversion. Notably, when comparing materials with similar morphologies, an increase in Cu content, to a limit, correlates with a higher alcohol production.<sup>55</sup> Ethanol is detected in the tubular materials containing copper, while in the flake-like materials, its formation is limited to samples with 40% and 50% Cu content. This suggests that both the copper concentration and material morphology play critical roles in determining the product distribution and efficiency.

The absence of a significant ethanol signal for the Cu30%-P123 catalyst is attributed to its substantially lower photocatalytic activity. This behavior is likely a consequence of the loss of the nanotubular morphology, which strongly affects charge transfer and intermediate stabilization. Although higher Cu contents (40–50%) can partially compensate for the lack of this morphology, enabling detectable ethanol formation, it is plausible that ethanol is still produced by Cu30%-P123 at rates below the detection limit of the GC-FID analysis employed.

Although these results point toward a morphology-dependent enhancement of methanol selectivity, the proposed "extended residence time" effect remains a working hypothesis. Further kinetic or in situ spectroscopic studies are required to confirm the confinement-driven mechanism responsible for the higher selectivity in tubular structures. Nevertheless, the higher methanol yield observed for Cu20%-P123 compared to Cu30%-P123 despite its lower Cu content supports the interpretation that the preserved nanotubular morphology promotes longer intermediate lifetimes and more efficient hydrogenation pathways. This interpretation is consistent with the findings of Wein et al., 54 who attributed the improved methanol selectivity in LDH-based photocatalysts to the prolonged residence time of intermediates confined within the interlayer or mesoporous domains.

**3.5.** Thermocatalytic  $CO_2$  Hydrogenation. Figure 8 presents the results of catalytic tests in thermocatalysis for the  $CO_2$  hydrogenation reaction. When materials with tubular and laminar structures were compared at the same Cu content (20%), it is evident that the tubular structure achieves higher methanol production. This is attributed to greater  $CO_2$  conversion and enhanced selectivity for methanol.

Moreover, XPS analysis revealed that the tubular material exhibits a higher  $Cu^0/Cu^+$  ratio on its surface, <sup>56</sup> which likely contributes to its superior catalytic performance. Both  $Cu^0$  and  $Cu^+$  active sites play a crucial role in promoting the reaction, as they are essential for the activation of the  $CO_2$  and hydrogenation pathways. This observation aligns with findings reported by Dong et al., <sup>51</sup> who demonstrated the importance of the  $Cu^0/Cu^+$  ratio in Cu-based materials for improving activity and selectivity during  $CO_2$  hydrogenation to methanol.

Additionally, Figure 7 illustrates a trend similar to that observed in photocatalysis, where the level of CO<sub>2</sub> conversion

**ACS Applied Nano Materials** 

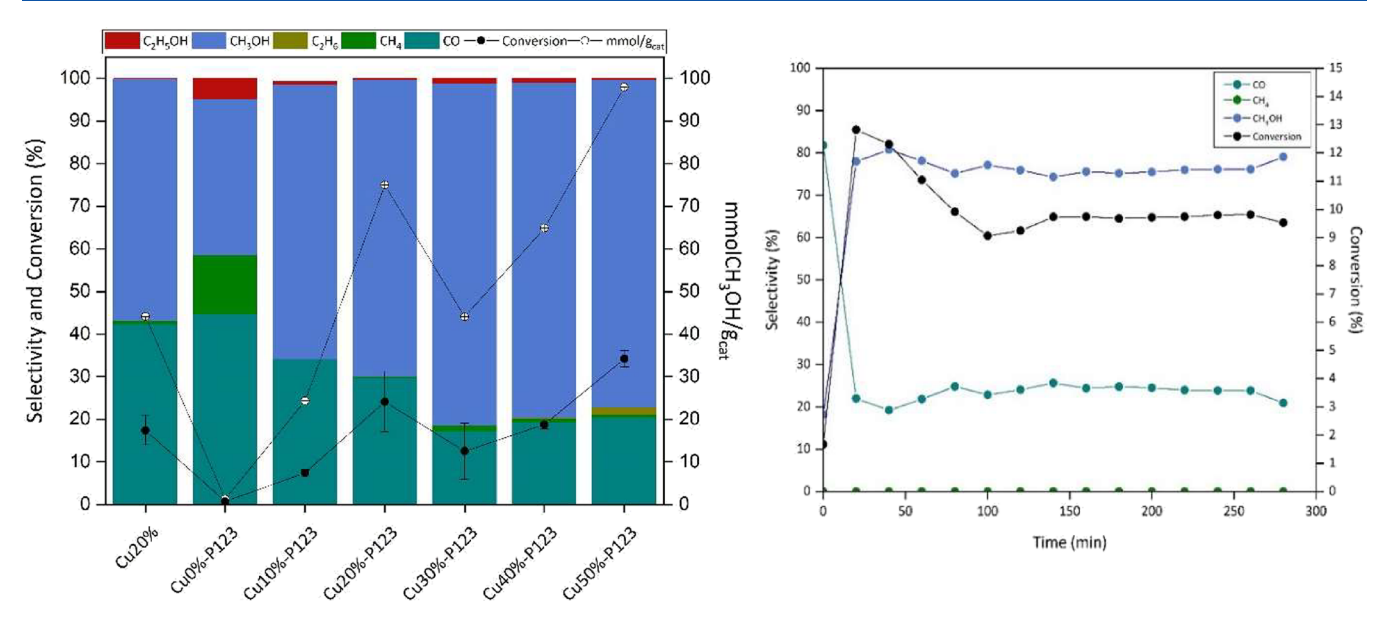


Figure 8. Left:  $CO_2$  conversion, selectivity, and methanol yield at various cooper-based catalysis. Reactions: 100 bar, 250 °C,  $CO_2/H_2$  molar ratio 1/4, 10 mg of catalyst, and 20h. Right: Conversion and selectivity of  $CO_2$  hydrogenation in a fixed-bed flow reactor, packed 1200 mg of Cu20%-P123, prereduced at 300 °C for 1h,  $CO_2$ : $H_2 = 1:4$ , GHSV = 2,5  $NLg_{cat}^{-1}h^{-1}$ .

increases as the Cu percentage rises from 0 to 20% in tubular materials. However, a decline in conversion is observed when the Cu percentage increases to 30%. This decrease is attributed to the inability to form well-defined nanotube structures when the Cu content exceeds 20%, which likely impacts the structural integrity and effectiveness of the catalyst. Despite this, a further increase in Cu percentage promotes higher conversion due to the enhanced catalytic activity, provided by the greater amount of Cu available on the catalyst surface. This suggests a balance between maintaining the desired nanotube morphology and optimizing the Cu content to achieve the highest catalytic performance.

Regarding methanol selectivity, it improves with an increasing Cu percentage, though there is a slight drop from 79 to 77% when the Cu percentage rises from 40 to 50%. This decrease is due to the higher amount of Cu promoting the formation of light hydrocarbons (CH<sub>4</sub> and C<sub>2</sub>H<sub>6</sub>). Nevertheless, the high conversion achieved with this material allows for a substantial methanol yield, producing 98 mmol of methanol per gram of catalyst.

Given the results presented above, the 20%Cu-P123 catalyst was selected for flow testing, as shown in Figure 7. This catalyst exhibited a high methanol yield with no methane formation, a significant advantage considering methane's impact as a potent greenhouse gas. Compared with the batch reaction, the selectivity for methanol was notably higher. Literature reports on Cu-ZnO-Al<sub>2</sub>O<sub>3</sub>-based catalysts in flow reactors typically indicate lower methanol selectivity than the values achieved in this study. 52,53,57 Furthermore, the methanol yield obtained with the 20%Cu-P123 catalyst was impressive, reaching 5.5 mg·g<sub>at</sub><sup>-1</sup>·h<sup>-1</sup> (1.27 mmol.g<sub>cat</sub><sup>-1</sup>.h<sup>-1</sup>), significantly surpassing yields reported in the literature for equivalent gas hourly space velocity (GHSV). 58-60 When compared with other LDH-based catalysts, Cu20%-P123 exhibited a higher methanol selectivity while maintaining comparable CO2 conversions. Zhao et al. 49 investigated layered copper-based catalysts (CZA-LDO and CZA-ALDO) and reported CO2 conversions below 10% at 250 °C and 30 bar under a GHSV of 8 L·gcat<sup>-1</sup>·h<sup>-1</sup>, with methanol selectivities of approximately 50

and 30%, respectively. Li et al.<sup>61</sup> examined copper-zincgallium LDH catalysts with varying gallium contents and achieved CO<sub>2</sub> conversions of 10-15%, with methanol selectivities below 60%, using a GHSV of 18 L·gcat<sup>-1</sup>·h<sup>-1</sup>. Similarly, Cui et al.<sup>62</sup> studied Cu-Zn-Al LDH catalysts for CO<sub>2</sub> hydrogenation to methanol and reported a 17% CO<sub>2</sub> conversion with 50% methanol selectivity at 30 bar, 250 °C, and a GHSV of 3.6 L·gcat<sup>-1</sup>·h<sup>-1</sup>. The experimental setup, depicted in Figure 8, involved CO2 hydrogenation in a fixedbed flow reactor packed with 1200 mg of Cu20%-P123 catalyst prereduced at 300 °C for 1 h. The reaction was conducted with a  $CO_2$ :H<sub>2</sub> ratio of 1:4 and a GHSV of 2.5  $NL \cdot g_{at}^{-1} \cdot h^{-1}$ , demonstrating the superior performance of this catalyst under optimized flow conditions. It is worth noting that the methanol yields discussed in this work are compared with literature data obtained under similar supercritical CO<sub>2</sub>:H<sub>2</sub> conditions. <sup>51–53</sup> In thermocatalytic systems, the supercritical state arises naturally from the elevated temperatures and pressures required to drive CO<sub>2</sub> hydrogenation, which exceed the critical temperature and pressure of the CO<sub>2</sub>/H<sub>2</sub> mixture. Therefore, our comparative analysis remains consistent with previous reports employing supercritical reaction media.

Our results suggest that two key factors synergistically govern ethanol formation under photocatalytic conditions: the catalyst morphology and its copper concentration. The nanotubular structure provides an optimal configuration for C–C coupling, allowing for efficient ethanol formation at relatively low Cu loadings (e.g., Cu20%-P123). In contrast, catalysts lacking this morphology require higher Cu contents to achieve comparable activity, as observed for Cu40%-P123 and Cu50%-P123. Therefore, the absence of ethanol for Cu30%-P123 reflects a composition—morphology mismatch, where the Cu loading is insufficient to compensate for the loss of nanotubular architecture.

# CONCLUSIONS

This study demonstrates that compositional and morphological tuning of LDHs through Eu<sup>3+</sup>-induced nanotubular

structuring and addition of Cu active sites markedly enhances the catalytic performance in CO<sub>2</sub> hydrogenation to methanol. In particular, the Cu20%-P123 LDH nanotubes reached a BET surface area of 184  $\rm m^2 \cdot g^{-1}$  and achieved methanol yields of up to 28  $\mu \rm mol \cdot g^{-1}$  under photocatalytic conditions and 98 mmol-  $\rm g^{-1}$  in thermocatalysis, significantly surpassing conventional Cu-ZnO-Al<sub>2</sub>O<sub>3</sub> catalysts. The superior activity and selectivity are attributed to the synergy among the nanotubular morphology, high surface area, and the coexistence of Cu<sup>0</sup>/Cu<sup>+</sup> active sites. These results highlight the potential of nanotubular LDHs as a platform for designing next-generation CO<sub>2</sub>-to-methanol catalysts.

While the nanotubular morphology has been shown to play a critical role in enhancing  $\mathrm{CO}_2$ -to-alcohol conversion, it is important to note that this effect cannot be directly extrapolated to other materials with similar geometries. For instance, Cu-doped carbon nanotubes might not exhibit comparable activity, as the synergy among Cu, Zn, and Al cations in the LDH framework is fundamental for stabilizing reaction intermediates and promoting selective hydrogenation. Therefore, the remarkable catalytic performance reported here arises from the unique interplay between morphology and composition rather than morphology alone.

#### ASSOCIATED CONTENT

## Supporting Information

The Supporting Information is available free of charge at https://pubs.acs.org/doi/10.1021/acsanm.5c03394.

Chemical analysis of LDHs with partial replacement of Cu Lattice parameters a and c of LDHs, concentration and elemental composition according to XPS data, FT-IR analysis, thermogravimetric curves of the ZnAl LDHs, UV—vis analysis, photoluminescence spectroscopy, and flowchart of the LDH nanotube preparation process (PDF)

### AUTHOR INFORMATION

## **Corresponding Author**

Danilo Mustafa — Instituto de Física da Universidade de São Paulo, São Paulo, SP 05508-090, Brazil; o orcid.org/0000-0001-5453-1737; Email: dmustafa@if.usp.br

#### **Authors**

Alexandre C. Teixeira — Instituto de Física da Universidade de São Paulo, São Paulo, SP 05508-090, Brazil

Bruno Manduca — Department of Fundamental Chemistry, Institute of Chemistry, University of São Paulo, São Paulo 05508-000, Brazil; o orcid.org/0000-0003-3457-9551

Adolfo L. Figueredo – Department of Fundamental Chemistry, Institute of Chemistry, University of São Paulo, São Paulo 05508-000, Brazil

Alysson F. Morais – Instituto de Física da Universidade de São Paulo, São Paulo, SP 05508-090, Brazil

Renato S. Freire – Department of Fundamental Chemistry, Institute of Chemistry, University of São Paulo, São Paulo 05508-000, Brazil

Pedro Vidinha – Department of Fundamental Chemistry, Institute of Chemistry, University of São Paulo, São Paulo 05508-000, Brazil; oorcid.org/0000-0002-3907-4969

Complete contact information is available at: https://pubs.acs.org/10.1021/acsanm.5c03394

#### **Author Contributions**

A.C.T.: Conceptualization, methodology, investigation, formal analysis, data curation, validation, visualization, writing—original draft, and writing—review and editing. A.F.M. Conceptualization, writing—review and editing, and funding acquisition. A.L.F., B.M., and R.S.F.: Data curation, validation, visualization, and writing—review and editing. P.V.: Methodology, resources, supervision, and writing—review and editing. D.M.: Conceptualization, methodology, resources, supervision, and writing—review and editing.

#### **Funding**

The Article Processing Charge for the publication of this research was funded by the Coordenacao de Aperfeicoamento de Pessoal de Nivel Superior (CAPES), Brazil (ROR identifier: 00x0ma614).

#### Notes

The authors declare no competing financial interest.

#### ACKNOWLEDGMENTS

D.M. acknowledges the Laboratory of Crystallography (IFUSP, São Paulo) for assistance with the PXRD measurements. P.V. acknowledges the support of the RCGI — Research Centre for Greenhouse Gas Innovation, hosted by the University of São Paulo (USP) and Shell Brazil, and the strategic importance of the support given by ANP (Brazil's National Oil, Natural Gas and Biofuels Agency) through the R&DI levy regulation. This research was funded by Fundação de Amparo à Pesquisa do Estado de São Paulo (FAPESP, 2014/50279-4; 2015/19210-0; 2018/13837-0; 2020/15230-5; 2022/01314-8 and 2025/00720-0).

#### **■** REFERENCES

- (1) International Energy Agency. CO<sub>2</sub> Capture and Utilisation. https://www.iea.org/energy-system/carbon-capture-utilisation-and-storage/co2-capture-and-utilisation (accessed May 11, 2025).
- (2) Zulqarnain; Mohd Yusoff, M. H.; Keong, L. K.; Yasin, N. H.; Rafeen, M. S.; Hassan, A.; Srinivasan, G.; Yusup, S.; Shariff, A. M.; Jaafar, A. B. Recent Development of Integrating CO <sub>2</sub> Hydrogenation into Methanol with Ocean Thermal Energy Conversion (OTEC) as Potential Source of Green Energy. *Green Chem. Lett. Rev.* 2023, 16 (1), No. 2152740.
- (3) Ye, R.-P.; Ding, J.; Gong, W.; Argyle, M. D.; Zhong, Q.; Wang, Y.; Russell, C. K.; Xu, Z.; Russell, A. G.; Li, Q.; Fan, M.; Yao, Y.-G. CO2 Hydrogenation to High-Value Products via Heterogeneous Catalysis. *Nat. Commun.* **2019**, *10* (1), 5698.
- (4) Patil, T.; Naji, A.; Mondal, U.; Pandey, I.; Unnarkat, A.; Dharaskar, S. Sustainable Methanol Production from Carbon Dioxide: Advances, Challenges, and Future Prospects. *Environ. Sci. Pollut. Res.* **2024**, *31* (32), 44608–44648.
- (5) Ruland, H.; Song, H.; Laudenschleger, D.; Stürmer, S.; Schmidt, S.; He, J.; Kähler, K.; Muhler, M.; Schlögl, R. CO 2 Hydrogenation with Cu/ZnO/Al 2 O 3: A Benchmark Study. *ChemCatChem.* **2020**, 12 (12), 3216–3222.
- (6) Kattel, S.; Ramírez, P. J.; Chen, J. G.; Rodriguez, J. A.; Liu, P. Active Sites for CO <sub>2</sub> Hydrogenation to Methanol on Cu/ZnO Catalysts. *Science* (1979) **2017**, 355 (6331), 1296–1299.
- (7) Liang, B.; Ma, J.; Su, X.; Yang, C.; Duan, H.; Zhou, H.; Deng, S.; Li, L.; Huang, Y. Investigation on Deactivation of Cu/ZnO/Al  $_2$  O  $_3$  Catalyst for CO  $_2$  Hydrogenation to Methanol. *Ind. Eng. Chem. Res.* **2019**, 58 (21), 9030–9037.
- (8) Zhang, W.; Ma, D.; Pérez-Ramírez, J.; Chen, Z. Recent Progress in Materials Exploration for Thermocatalytic, Photocatalytic, and Integrated Photothermocatalytic CO 2 -to-Fuel Conversion. *Advanced Energy and Sustainability Research* **2022**, 3 (2), No. 2100169.

- (9) Kovačič, Ž.; Likozar, B.; Huš, M. Photocatalytic CO<sub>2</sub> Reduction: A Review of Ab Initio Mechanism, Kinetics, and Multiscale Modeling Simulations. ACS Catal. **2020**, 10 (24), 14984–15007.
- (10) Gothe, M. L.; Pérez-Sanz, F. J.; Braga, A. H.; Borges, L. R.; Abreu, T. F.; Bazito, R. C.; Gonçalves, R. V.; Rossi, L. M.; Vidinha, P. Selective CO2 Hydrogenation into Methanol in a Supercritical Flow Process. J. CO2 Util 2020, 40, No. 101195.
- (11) Shen, C.; Sun, K.; Zou, R.; Wu, Q.; Mei, D.; Liu, C. CO <sub>2</sub> Hydrogenation to Methanol on Indium Oxide-Supported Rhenium Catalysts: The Effects of Size. ACS Catal. **2022**, 12 (20), 12658–12669.
- (12) Zhao, L.; Zhang, L.; Wu, Z.; Huang, C.; Chen, K.; Wang, H.; Yang, F. Size Effect of Cu Particles on Interface Formation in Cu/ZnO Catalysts for Methanol Synthesis. *Catalysts* **2023**, *13* (8), 1190.
- (13) Choi, H.; Oh, S.; Trung Tran, S. B.; Park, J. Y. Size-Controlled Model Ni Catalysts on Ga2O3 for CO2 Hydrogenation to Methanol. *J. Catal.* **2019**, *376*, 68–76.
- (14) Barberis, L.; Hakimioun, A. H.; Plessow, P. N.; Visser, N. L.; Stewart, J. A.; Vandegehuchte, B. D.; Studt, F.; de Jongh, P. E. Competition between Reverse Water Gas Shift Reaction and Methanol Synthesis from CO 2: Influence of Copper Particle Size. *Nanoscale* **2022**, *14* (37), 13551–13560.
- (15) Yang, B.; Chen, X.; Guo, L.; Zhang, L. Catalyst Architecture for Metal-Support Interactions and Its Effects on Heterogeneous Reactions. *J. Mater. Chem. A Mater.* **2024**, *12* (31), 19861–19884.
- (16) Yim, C. M.; Pang, C. L.; Hermoso, D. R.; Dover, C. M.; Muryn, C. A.; Maccherozzi, F.; Dhesi, S. S.; Pérez, R.; Thornton, G. Influence of Support Morphology on the Bonding of Molecules to Nanoparticles. *Proc. Natl. Acad. Sci. U.S.A.* **2015**, *112* (26), 7903–7908.
- (17) Engel, J.; Francis, S.; Roldan, A. The Influence of Support Materials on the Structural and Electronic Properties of Gold Nanoparticles a DFT Study. *Phys. Chem. Chem. Phys.* **2019**, *21* (35), 19011–19025.
- (18) Barkaoui, S.; Wang, Y.; Zhang, Y.; Gu, X.; Li, Z.; Wang, B.; Baiker, A.; Li, G.; Zhao, Z. Critical Role of NiO Support Morphology for High Activity of Au/NiO Nanocatalysts in CO Oxidation. *iScience* **2024**, 27 (7), No. 110255.
- (19) Lee, K.; Yan, H.; Sun, Q.; Zhang, Z.; Yan, N. Mechanism-Guided Catalyst Design for CO <sub>2</sub> Hydrogenation to Formate and Methanol. *Acc. Mater. Res.* **2023**, 4 (9), 746–757.
- (20) Araújo, T. P.; Mitchell, S.; Pérez-Ramírez, J. Design Principles of Catalytic Materials for CO <sub>2</sub> Hydrogenation to Methanol. *Adv. Mater.* **2024**, 36 (48), No. 2409322.
- (21) Jiang, X.; Nie, X.; Guo, X.; Song, C.; Chen, J. G. Recent Advances in Carbon Dioxide Hydrogenation to Methanol via Heterogeneous Catalysis. *Chem. Rev.* **2020**, *120* (15), 7984–8034.
- (22) Mori, K.; Taga, T.; Yamashita, H. Isolated Single-Atomic Ru Catalyst Bound on a Layered Double Hydroxide for Hydrogenation of CO<sub>2</sub> to Formic Acid. ACS Catal. **2017**, 7 (5), 3147–3151.
- (23) Miao, P.; Zhao, J.; Shi, R.; Li, Z.; Zhao, Y.; Zhou, C.; Zhang, T. Layered Double Hydroxide Engineering for the Photocatalytic Conversion of Inactive Carbon and Nitrogen Molecules. *ACS ES&T Engineering* **2022**, *2* (6), 1088–1102.
- (24) Szabados, M.; Szabados, T.; Mucsi, R.; Baán, K.; Kiss, J.; Szamosvölgyi, Á.; Sápi, A.; Kónya, Z.; Kukovecz, Á.; Sipos, P. Directed Thermocatalytic CO2 Reduction over NiAl4 Layered Double Hydroxide Precursors Activity and Selectivity Control Using Different Interlayer Anions. J. CO2 Util 2023, 75, No. 102567.
- (25) Huang, J.; Zhang, Z.; Wei, Y.; Guo, L.; Liu, J.; Zhang, C.; Xue, Z.; Sun, S. Layered Double Hydroxides Derived CuFe-Based Catalysts for CO2 Hydrogenation to Long-Chain Hydrocarbons. *Chem. Inorg. Mater.* **2023**, *1*, No. 100004.
- (26) Gil-Gavilán, D. G.; Cosano, D.; Amaro-Gahete, J.; Castillo-Rodríguez, M.; Esquivel, D.; Ruiz, J. R.; Romero-Salguero, F. J. Zn-Cr Layered Double Hydroxides for Photocatalytic Transformation of CO2 under Visible Light Irradiation: The Effect of the Metal Ratio and Interlayer Anion. *Catalysts* **2023**, *13* (10), 1364.
- (27) Li, Z.; Shi, R.; Zhao, J.; Zhang, T. Ni-Based Catalysts Derived from Layered-Double-Hydroxide Nanosheets for Efficient Photo-

- thermal CO2 Reduction under Flow-Type System. Nano Res. 2021, 14 (12), 4828-4832.
- (28) Morais, A. F.; Silva, I. G. N. N.; Sree, S. P.; de Melo, F. M.; Brabants, G.; Brito, H. F.; Martens, J. A.; Toma, H. E.; Kirschhock, C. E. A. A.; Breynaert, E.; Mustafa, D. Hierarchical Self-Supported ZnAlEu LDH Nanotubes Hosting Luminescent CdTe Quantum Dots. Chem. Commun. 2017, 53 (53), 7341–7344.
- (29) Teixeira, A. C.; Nunes Silva, I. G.; Morais, A. F.; Mustafa, D. Structural and Optical Properties of Pillared Eu3+-Containing Layered Double Hydroxides Intercalated by 2- to 12-Carbon Aliphatic Dicarboxylates. *J. Rare Earths* **2022**, *40* (2), 260–267.
- (30) Teixeira, A.; Morais, A.; Silva, I.; Breynaert, E.; Mustafa, D. Luminescent Layered Double Hydroxides Intercalated with an Anionic Photosensitizer via the Memory Effect. *Crystals (Basel)* **2019**, 9 (3), 153.
- (31) Teixeira, A. C.; Netzlaff Fachini, N. F.; Kakinami, H. K. C.; Mustafa, D. Efficient Energy Transfer in Eu  $^{3+}$  -Doped Layered Double Hydroxides with  $\beta$ -Diketonate Anions Obtained by the Memory Effect. *ACS Omega* **2025**. *10* 44137 .
- (32) Zhao, Y.; Li, Z.; Li, M.; Liu, J.; Liu, X.; Waterhouse, G. I. N.; Wang, Y.; Zhao, J.; Gao, W.; Zhang, Z.; Long, R.; Zhang, Q.; Gu, L.; Liu, X.; Wen, X.; Ma, D.; Wu, L.; Tung, C.; Zhang, T. Reductive Transformation of Layered-Double-Hydroxide Nanosheets to Fe-Based Heterostructures for Efficient Visible-Light Photocatalytic Hydrogenation of CO. Adv. Mater. 2018, 30 (36), No. 1803127.
- (33) Chen, G.; Gao, R.; Zhao, Y.; Li, Z.; Waterhouse, G. I. N.; Shi, R.; Zhao, J.; Zhang, M.; Shang, L.; Sheng, G.; Zhang, X.; Wen, X.; Wu, L.; Tung, C.; Zhang, T. Alumina-Supported CoFe Alloy Catalysts Derived from Layered-Double-Hydroxide Nanosheets for Efficient Photothermal CO <sub>2</sub> Hydrogenation to Hydrocarbons. *Adv. Mater.* **2018**, *30* (3).
- (34) Zhao, Y.; Zhao, Y.; Waterhouse, G. I. N.; Zheng, L.; Cao, X.; Teng, F.; Wu, L.; Tung, C.; O'Hare, D.; Zhang, T. Layered-Double-Hydroxide Nanosheets as Efficient Visible-Light-Driven Photocatalysts for Dinitrogen Fixation. *Adv. Mater.* **2017**, 29 (42), No. 1703828.
- (35) Silva, C. G.; Bouizi, Y.; Fornés, V.; García, H. Layered Double Hydroxides as Highly Efficient Photocatalysts for Visible Light Oxygen Generation from Water. *J. Am. Chem. Soc.* **2009**, *131* (38), 13833–13839.
- (36) Zhao, Y.; Chen, P.; Zhang, B.; Su, D. S.; Zhang, S.; Tian, L.; Lu, J.; Li, Z.; Cao, X.; Wang, B.; Wei, M.; Evans, D. G.; Duan, X. Highly Dispersed TiO6 Units in a Layered Double Hydroxide for Water Splitting. *Chem. Eur. J.* **2012**, *18* (38), 11949–11958.
- (37) Ahmed, N.; Morikawa, M.; Izumi, Y. Photocatalytic Conversion of Carbon Dioxide into Methanol Using Optimized Layered Double Hydroxide Catalysts. *Catal. Today* **2012**, *185* (1), 263–269.
- (38) Mor, G. K.; Shankar, K.; Paulose, M.; Varghese, O. K.; Grimes, C. A. Enhanced Photocleavage of Water Using Titania Nanotube Arrays. *Nano Lett.* **2005**, *5* (1), 191–195.
- (39) Ding, Z.; Zhu, H. Y.; Greenfield, P. F.; Lu, G. Q. Characterization of Pore Structure and Coordination of Titanium in TiO2 and SiO2-TiO2 SoI-Pillared Clays. *J. Colloid Interface Sci.* **2001**, 238 (2), 267–272.
- (40) Lei, X.; Lu, W.; Peng, Q.; Li, H.; Chen, T.; Xu, S.; Zhang, F. Activated MgAl-Layered Double Hydroxide as Solid Base Catalysts for the Conversion of Fatty Acid Methyl Esters to Monoethanolamides. *Appl. Catal. A Gen* **2011**, 399 (1–2), 87–92.
- (41) Álvarez, M. G.; Frey, A. M.; Bitter, J. H.; Segarra, A. M.; de Jong, K. P.; Medina, F. On the Role of the Activation Procedure of Supported Hydrotalcites for Base Catalyzed Reactions: Glycerol to Glycerol Carbonate and Self-Condensation of Acetone. *Appl. Catal., B* **2013**, 134–135, 231–237.
- (42) Morais, A. F.; Nanclares, D.; Silva, I. G. N.; Duarte, A.; Garcia, F. A.; Breynaert, E.; Mustafa, D. Mesostructuring Layered Materials: Self-Supported Mesoporous Layered Double Hydroxide Nanotubes. *Nanoscale* **2021**, *13* (27), 11781–11792.

- (43) Nanclares, D.; Morais, A. F.; Calaça, T.; Silva, I. G. N.; Mustafa, D. A Class of Novel Luminescent Layered Double Hydroxide Nanotubes. *RSC Adv.* **2021**, *11* (40), 24747–24751.
- (44) Morais, A. F.; Silva, I. G. N.; Lima, B. C.; Garcia, F. A.; Mustafa, D. Coordination of Eu3+Activators in ZnAlEu Layered Double Hydroxides Intercalated by Isophthalate and Nitrilotriacetate. *ACS Omega* **2020**, *5* (37), 23778–23785.
- (45) Silva, I. G. N.; Mustafa, D.; Felinto, M. C. F. C.; Faustino, W. M.; Teotonio, E. E. S.; Malta, O. L.; Brito, H. F. Low Temperature Synthesis of Luminescent RE 2 O 3: Eu 3+ Nanomaterials Using Trimellitic Acid Precursors. *J. Braz Chem. Soc.* **2015**, 26 (12), 2629–2639
- (46) Prašnikar, A.; Pavlišič, A.; Ruiz-Zepeda, F.; Kovač, J.; Likozar, B. Mechanisms of Copper-Based Catalyst Deactivation during CO <sub>2</sub> Reduction to Methanol. *Ind. Eng. Chem. Res.* **2019**, 58 (29), 13021–13029
- (47) Wu, L.; Peng, B.; Li, Q.; Wang, Q.; Yan, X.; Li, K.; Lin, Q. Effects of Cu<sup>2+</sup> Incorporation on ZnAl-Layered Double Hydroxide. *New J. Chem.* **2020**, 44 (14), 5293–5302.
- (48) Yang, S.-q.; He, J.-p.; Zhang, N.; Sui, X.-w.; Zhang, L.; Yang, Z.-x. Effect of Rare-Earth Element Modification on the Performance of Cu/ZnAl Catalysts Derived from Hydrotalcite Precursor in Methanol Steam Reforming. *J. Fuel Chem. Technol.* **2018**, *46*, 179–188.
- (49) Zhao, F.; Fan, L.; Xu, K.; Hua, D.; Zhan, G.; Zhou, S. F. Hierarchical Sheet-like Cu/Zn/Al Nanocatalysts Derived from LDH/MOF Composites for CO2 Hydrogenation to Methanol. *Journal of CO2 Utilization* **2019**, 33, 222–232.
- (50) Santos, R. M. M.; Briois, V.; Martins, L.; Santilli, C. V. Insights into the Preparation of Copper Catalysts Supported on Layered Double Hydroxide Derived Mixed Oxides for Ethanol Dehydrogenation. *ACS Appl. Mater. Interfaces* **2021**, *13* (22), 26001–26012.
- (51) Dong, X.; Li, F.; Zhao, N.; Xiao, F.; Wang, J.; Tan, Y. CO2 Hydrogenation to Methanol over Cu/ZnO/ZrO2 Catalysts Prepared by Precipitation-Reduction Method. *Appl. Catal., B* **2016**, *191*, 8–17.
- (52) Śloczyński, J.; Grabowski, R.; Kozłowska, A.; Olszewski, P.; Stoch, J.; Skrzypek, J.; Lachowska, M. Catalytic Activity of the M/(3ZnO·ZrO2) System (M = Cu, Ag, Au) in the Hydrogenation of CO2 to Methanol. *Appl. Catal. A Gen* **2004**, 278 (1), 11–23.
- (53) Martin, O.; Mondelli, C.; Cervellino, A.; Ferri, D.; Curulla-Ferré, D.; Pérez-Ramírez, J. Operando Synchrotron X-ray Powder Diffraction and Modulated-Excitation Infrared Spectroscopy Elucidate the CO 2 Promotion on a Commercial Methanol Synthesis Catalyst. *Angew. Chem., Int. Ed.* **2016**, *55* (37), 11031–11036.
- (54) Anton Wein, L.; Zhang, H.; Urushidate, K.; Miyano, M.; Izumi, Y. Optimized Photoreduction of CO2 Exclusively into Methanol Utilizing Liberated Reaction Space in Layered Double Hydroxides Comprising Zinc, Copper, and Gallium. *Appl. Surf. Sci.* **2018**, 447, 687–696.
- (55) Li, Y.; Zhang, W.; Shen, X.; Peng, P.; Xiong, L.; Yu, Y. Octahedral Cu2O-Modified TiO2 Nanotube Arrays for Efficient Photocatalytic Reduction of CO2. *Chin. J. Catal.* **2015**, *36* (12), 2229–2236.
- (56) Pacchioni, G. From CO 2 to Methanol on Cu/ZnO/Al 2 O 3 Industrial Catalyst. What Do We Know about the Active Phase and the Reaction Mechanism? *ACS Catal.* **2024**, *14* (4), 2730–2745.
- (57) Martin, O.; Martín, A. J.; Mondelli, C.; Mitchell, S.; Segawa, T. F.; Hauert, R.; Drouilly, C.; Curulla-Ferré, D.; Pérez-Ramírez, J. Indium Oxide as a Superior Catalyst for Methanol Synthesis by CO 2 Hydrogenation. *Angew. Chem. Inter. Ed.* **2016**, 55 (21), 6261–6265.
- (58) Bonura, G.; Arena, F.; Mezzatesta, G.; Cannilla, C.; Spadaro, L.; Frusteri, F. Role of the Ceria Promoter and Carrier on the Functionality of Cu-Based Catalysts in the CO2-to-Methanol Hydrogenation Reaction. *Catal. Today* **2011**, *171* (1), 251–256.
- (59) Choi, E. J.; Lee, Y. H.; Lee, D.-W.; Moon, D.-J.; Lee, K.-Y. Hydrogenation of CO2 to Methanol over Pd-Cu/CeO2 Catalysts. *Molecular Catalysis* **2017**, 434, 146–153.
- (60) Chang, K.; Wang, T.; Chen, J. G. Hydrogenation of CO2 to Methanol over CuCeTiO Catalysts. *Appl. Catal., B* **2017**, 206, 704–711.

- (61) Li, M. M. J.; Chen, C.; Ayvall, T.; Suo, H.; Zheng, J.; Teixeira, I. F.; Ye, L.; Zou, H.; O'Hare, D.; Tsang, S. C. E. CO2 Hydrogenation to Methanol over Catalysts Derived from Single Cationic Layer CuZnGa LDH Precursors. ACS Catal. 2018, 8 (5), 4390–4401.
- (62) Cui, X.; Luo, M.; Yang, Z.; Rahman, R.; Li, Z.; Yang, W.; Xia, L. Efficient Cu-Zn-Al/LDH Catalysts for CO2-to-Methanol Conversion. *Energy Fuels* **2025**, *39* (5), 2675–2687.

